Automatic microseismic stacking location with a multi-cross-correlation imaging condition

Congcong Yuan[1], Wei Zhang[2], Jie Zhang[1]

[1]Geophysical Research Institute, School of Earth and Space Sciences, University of

Science and Technology of China, Hefei, Anhui 230026, P. R. China

[2]School of Earth and Space Sciences, Southern University of Science and Technology,

Shenzhen, Guangdong 518055, P. R. China

Congcong Yuan: congcy@mail.ustc.edu.cn

Wei Zhang: zhangwei@sustc.edu.cn

Jie Zhang: jzhang25@ustc.edu.cn

ABSTRACT

Source scanning algorithm (SSA) has been recognized as a valid technique to automatically detect and locate passive seismic events. The imaging condition of this algorithm is the linear stack of the amplitudes along the traveltime curve from trial locations. However, the linear stacking condition may cause the location uncertainty due to the polarity reversal and low signal-to-noise ratio of the recorded waveforms. To alleviate these uncertainties, under the assumption of dense survey geometry on the surface, we introduce the cross-correlation condition and further propose a new condition named as multi-cross-correlation, which is implemented by accumulatively multiplying the amplitude on each receiver or receiver group. In the analysis of the comparisons with the linear condition, both cross-correlation and multi-cross-correlation conditions are effective to avoid the location uncertainties resulting from the polarity reversal, and the multi-cross-correlation is the most robust and effective to suppress the noise and reduce the location uncertainties among these conditions. However, same to linear condition, other two conditions are also sensitive to the velocity uncertainty at the depth of event location. Field data example suggests that cross-correlation and multi-cross-correlation conditions would produce more reasonable location results than linear condition does.

Keywords: Source stacking algorithm; Cross-correlation; Multi-cross-correlation; Passive seismic location

INTRODUCTION

Currently, microseismic monitoring has been widely applied in many fields, such as fault belts (Hermann et al., 2011), volcanic activities (Roman and Cashman, 2006), landslide-prone regions (Got et al., 2010), mining (Li and Zhao, 2012), tunnel excavation (Feng et al., 2012), and geothermal and hydrocarbon reservoirs (Suckale, 2009). During the monitoring, parameters of detected microseismic events are utilized to delineate the distribution and shape of fracture network. For the hydraulic stimulation, these characteristics can be used to interpret fracturing efficiency as well as adjust treatment design and evaluate the stimulated reservoir volume better (Li et al., 2014; Grechka et al., 2015).

The borehole and surface observation arrays are two available ways to monitor microseismicity. The downhole monitoring has records with higher signal-to-noise ratio (S/N), but has limited spatial coverage of the receivers and hence the horizontal location of the events is not well constrained (Eisner et al., 2009, 2010; Muller, 2013). In contrast, the surface survey usually has lower S/N but better horizontal resolution, while the depth uncertainty is larger due to lack of constraint in the depth (Duncan and Eisner, 2010). Because of the low S/N of surface recordings, stacking location methods are preferred rather than traditional picking-based location methods (Geiger, 1912; Rutledge and Phillips, 2003; Akram and Eaton, 2016).

There are three available in-time and in-situ location techniques developed for surface monitoring. One is diffraction stacking imaging approaches (Kao and Shan, 2004; Baker et al., 2005; Rentsch et al., 2007; Gajewski et al., 2007; Grigolia et al.,

2013; Hadorsen et al., 2013; Zhang and Zhang, 2013), Kao and Shan (2004) presented SSA in which the traveltime table for the potential location grids was calculated in advance, and then the SSA was applied to stack the amplitudes along the traveltime curve of all receivers and search the grid with the maximum stacking energy, which would be regarded as the event location. Baker et al. (2005) suggested to use envelops of seismograms. Gajewski et al. (2007) developed a migration-type approach with the back-projection of the seismic recordings. Rentsch et al. (2007) applied the stacking strategy to the energy of three-component (3C) data weighted with a Gaussian-beam-type factor. Grigoli et al. (2013) proposed to stack the short time average to long time average ratio (STA/LTA) traces. For elastic waves, Haldorsen et al. (2013) proposed the deconvolution imaging condition and Zhang and Zhang (2013) developed the cross-component cross-correlation imaging condition to extract the coherence of P- and S-waves. The second type of techniques is reverse time imaging (RTI) approaches (McMechan, 1982; Gajewski and Tessmer, 2005; Artman et al., 2010; Witten and Artman, 2012; Fish, 2012; Wu et al., 2017). Gajewski and Tessmer (2005) showed that the energy could be refocused by backward propagating the wavefields (McMechan, 1982). The extrapolated wavefields are in 4D (time and space) due to unknown origin time, hence, a reasonably focused image for the event location can be searched in the 4D cube (Fish, 2012). Artman et al. (2010) and Witten and Artman (2011) generalized this approach using P- and S- waves based on zero-lag cross-correlation condition. The third type of techniques is full waveform inversion (Wu and McMechan, 1996；Minkoff and Symes, 1997; Ramos-Martinez and McMechan, 2001; Kaderli et al., 2015; Michel

and Tsvankin, 2014a,b, 2016; Huang et al., 2017). Minkoff and Symes (1997) applied full waveform inversion (FWI) to invert for both the mechanical earth parameters and the seismic source. Wu and McMechan (1996) used FWI to determine the spatial coordinates and origin time as well as the amplitude and angle associated with the double-couple. Ramos-Martinez and McMechan (2001) estimated source parameters via FWI in viscoelastic, anisotropic media. Michel and Tsvankin (2014a, b) used FWI to invert for the spatial coordinates and origin time as well as the moment tensors, and extended to the anisotropic case (Michel and Tscankin, 2016). These methods are appealing because they make use of waveforms, without requiring any manual picks of phase-arrivals. Compared to the RTI-based and FWI-based methods that are still in development due to its intensive computation for solving the wave equation, SSA has been proven as a stable and efficient tool to monitor slow earthquake and also for induced seismicity in oil and gas industry (Kao et al., 2006; Liao et al., 2012), while it only uses P- and/or S-phases rather than the whole wavefield.

However, the surface monitoring for SSA may encounter some uncertainty challenges, such as low S/R and polarity reversal. Because of the weak energy of the microseismic event and strong attenuation of shallow weathering layers, the S/N of the recordings may be such small that the estimation of the final location is affected severely (Eisner et al, 2009; Thornton et al., 2011). In the diffraction stacking based methods, the problem of changing polarities (due to the radiation pattern of source mechanism) remains unavoidable. To overcome the destructive interference, the polarity is usually determined through estimating moment tensors before stacking

(Anikiev et al., 2014; Zhebel and Eisner, 2015; Vlcek et al., 2016; Liang et al., 2016). Besides, the cross-correlation technique is often employed in order to evaluate the coherencies between wavefroms from different sources or stations and hence mitigate the location uncertainty. Hulsey et al. (2009) utilized a relative location technique (Eisner et al., 2008) to relatively locate induced microseismic events. Li et al. (2015) proposed a weighted-elastic-wave interferometric imaging to locate multiple sources with high location precision. Both approaches need to cross-correlate two recorded traces from the event or receiver pair before stacking. The cross-correlation between different waveforms will largely enhance the computation cost, while pairing different waveforms augment the available information for improving the location accuracy. In this study, we conduct the cross-correlation condition directly to calculate the energy brightness instead of the original linear stacking condition (Kao and Shan, 2004). Different from achieving the cross-correlated data before stacking, we calculate the coherencies between all neighboring receivers during stacking. We further develop a multi-cross-correlation condition for the energy brightness calculation on the coherencies among all receivers or possible receiver groups. By assuming that the survey geometry is densely set up, both correlation-based conditions enable the stacking algorithm to eliminate the influence of polarity reversals without extra computational cost. We shall first introduce the theory of both cross-correlation and multi-cross-correlation stacking conditions. We then present and analyze the results from the conventional linear condition and both introduced conditions in the account of polarity reversal and low SNR. Further, we apply these conditions to a real case study

for microseismic data processing.

METHODS

The SSA has been introduced by Kao and Shan (2004) to image the distribution of seismic sources in both time and space using trial locations and origin times. The 'brightness' function or linear stacking condition is used to calculate the energy value by summing the absolute amplitudes observed at all stations at their respective predicted arrival times. The locations of events are then identified by a systematic search throughout the whole spatial and temporal energy distribution for the maximum energy or brightness. We view the spatio-temporal distribution as the event location image. The location accuracy and precision may depend on the resolution of the event location image, which may be subjected to the stack condition. The original condition proposed by Kao and Shan (2004) is the linear stacking defined as,

$$E(t_0, x, y, z) = \sum_{ic=0}^{nc-1} \sum_{ir=0}^{nr-1} \left| A_{nr \cdot ic + ir} \left(t^{ir} (t_0, x, y, z) \right) \right| \tag{1}$$

where t_0 is the origin time of the source, x, y and z denote three dimensions of the source location. $t(t_0, x, y, z)$ is the predicted arrival time. nc represents the number of observation components, $1c$ or $3c$. nr stands for the number of receivers. A denotes the amplitude of the waveform data. For explosive sources, the linear stack imaging condition can reasonably focus the source location as the maximum energy point in the temporal and spatial cube. However, most of the microseismic events have nonexplosive components and their radiation patterns have similar characteristics as

earthquakes, thus the polarities of the amplitudes at different receivers may be inconsistent due to source mechanism. If the above localization approach is applied to pure double-couple sources, the stacked results are ambiguous because several maximas are present in the location image, which does not correspond to the true source location (Artman et al., 2010). To overcome this problem and obtain a higher resolution location image, we attempt to apply the cross-correlation to the adjacent receivers directly during stacking and the condition can be expressed as,

$$E(t_0, x, y, z) = \sum_{ic=0}^{nc-1} \sum_{ir=0}^{nr-2} \left| A_{nr \cdot ic+ir} \left(t^{ir} \left(t_0, x, y, z \right) \right) \cdot A_{nr \cdot ic+ir+1} \left(t^{ir+1} \left(t_0, x, y, z \right) \right) \right| \tag{2}$$

Note that the implementation of this condition is different from the interferometric imaging where the cross-correlated data is produced before stacking (Li et al., 2015). During this implementation, we directly multiply the amplitudes at the neighboring receivers and then summing all products up as the above equation. For the two-receiver case, we obtain a 4D stacking function $E(t_0, x, y, z)$. At the true event position, its stacking function is simply presented as,

$$E\left(t_0, x_0, y_0, z_0 \right) = A_i \left(t^i \left(t_0, x_0, y_0, z_0 \right) \right) \cdot A_j \left(t^j \left(t_0, x_0, y_0, z_0 \right) \right) \tag{3}$$

where $E\left(t_0, x_0, y_0, z_0 \right)$ is the maximum energy, which corresponds to the true position $\left(x_0, y_0, z_0 \right)$ and origin time t_0 of the source. i, j denote the receiver indexes. For simplicity, we assume that the source function is a delta function in the time domain, the convolution function between the observed data A_i and A_j is $G_i \cdot G_j$ in the frequency domain, where the component of high frequency is enhanced and hence the spatial resolution would be improved in the location image. If we consider the waveform polarity, we can rewrite the equation (3) as,

8

$$E\left(t_0, x_0, y_0, z_0\right) = \left(S_i \cdot A_i\left(t^i\left(t_0, x_0, y_0, z_0\right)\right)\right) \cdot \left(S_j \cdot A_j\left(t^j\left(t_0, x_0, y_0, z_0\right)\right)\right)$$
$$= \left(S_i \cdot S_j\right) \cdot \left(A_i\left(t^i\left(t_0, x_0, y_0, z_0\right)\right) \cdot A_j\left(t^j\left(t_0, x_0, y_0, z_0\right)\right)\right) \tag{4}$$

where S_i and S_j represent the waveform polarity of receiver i and j recordings, respectively. The dense surface array is usually deployed for microseismic monitoring (Duncan and Eisner, 2010). In these cases, most neighboring receivers share the same polarity, except for those across rupture planes. The production of neighboring receivers' polarities $S_i \cdot S_j$ is always positive in the same up- or down-section of the radiation pattern. It is unconcerned for those handful of neighboring receivers with opposite polarities in dense survey array. Hence, the problem of polarity reversal is effectively eliminated in the stacking location. Additionally, compared to using absolute values of the waveforms (Kao and Shan, 2004), the cross-correlation or product $A_i \cdot A_j$ suppresses noises and artifacts, thereby the resolution of the location imaging is improved. In the implementations of the cross-correlation condition, we find that this condition could not suppress the artifacts very effectively. It still causes large uncertainties in the location image, especially using the data in high noises. We shall show the results of synthetic experiments in the following section. In order to further improve the resolution of the location image while maintaining insensitive to radiation patterns, we propose the other correlation-based condition. Different from the cross-correlation condition, we multiply the amplitudes on all receivers by replacing summations and extend the equation (2) to the following as,

$$E(t_0, x, y, z) = \sum_{ic=0}^{nc-1} \left| \prod_{ir=0}^{nr-1} A_{nr \cdot ic + ir}\left(t^{ir}\left(t_0, x, y, z\right)\right) \right| \tag{5}$$

According to the (Arfken et al., 2013), the production of the equation above can

be regarded as multi-dimensional cross-correlation. We refer to the condition as multi-cross-correlation. Like the description by equation (4), we can extend two-receiver pair to multiple receivers. The production of multiple receivers enhances the resolution of the location imaging much more compared with the cross-correlation condition does. Meanwhile, the stacking function is insensitive to the polarity reversal whatever the type of microseismic source or event is, because we multiply all receiver recordings instead of summing them up. Nevertheless, if the observed signal on one receiver is close to zero, the final multiplication will be close to zero. To make our condition more robust and flexible, we divide the receivers into different groups, and then we multiply the summed amplitudes of all groups, which can be expressed as,

$$E(t_0, x, y, z) = \sum_{ic=0}^{nc-1} \prod_{ig=0}^{ng} \left| \sum_{ir=0}^{nr/ng-1} A_{nr\cdot ic+nr\cdot ig/ng+ir} \left(t^{nr\cdot ig/ng+ir} \left(t_0, x, y, z \right) \right) \right| \tag{6}$$

with ng is the number of receiver groups. If $ng = 1$, then the equation degrades as the linear stack condition; if $ng = nr$, then the equation is the same as equation (5). Here is a trade-off between the resolution and the stability of the location imaging. The resolution will increase with the group number increases, while the stability may decrease. To be robust and precise, we set $ng = 20$ in the following synthetic and real tests. The computation efficiency of the condition is almost the same as the linear stack and cross-correlation conditions from the perspective of the above formulas.

To be understood easily, we schematically describe three stacking conditions mentioned above in Figure 1. We assume that three receivers are deployed on the surface to record the event triggered at the location of x in space and origin time of t_0 in time. Above each station are the corresponding waveforms in which the predicted

arrival times of the largest amplitude A_t are labeled as dots. Provided the background velocity model, we can calculate the traveltime t from the trial event to each receiver. Then arrival times can be aligned to the waveforms for amplitudes, followed by using the stacking condition for the energy at each trial event. When the arrival times are consistent with the predicted arrival times, the maximum of energy (marked by filled circles) can be found at (x, t_0). Some artifacts are actually coexisted with the filled circles. We denote these artifacts as the arcs across those circles. The length of the arc means the severity of the artifact. Green, blue, and red colors represent the linear, cross-correlation, and multi-cross-correlation stacking conditions, respectively. The corresponding equations in Figure 1 are simplified versions of equations (1, 2, 5). With the equation of the third condition, we obviously know that the peak of the waveform will be enhanced a lot, in the meantime, the side lobes of the waveform will be weakened. The resolution will be therefore improved significantly in the energy map of source location compared with other two conditions. Similarly, the second condition will contribute to a higher resolution of source location than the first condition does. Meanwhile, if receivers are dense deployed on the surface, the correlation-based conditions are not sensitive to polarity reversals from the radiation pattern, since most adjacent receivers enjoy the same polarities. In the following, the synthetic and real cases will show the validity of the cross-correlation and multi-cross-correlation conditions.

SYNTHETIC EXAMPLES

In this section, we test three imaging conditions mentioned in the previous section and compare their imaging results under the circumstances of polarity reversal as well as noisy data. To analyze these effects on event locations, we first apply three imaging conditions in a pure test without any effect. Figure 2 shows a layered velocity model and the survey geometry designed for the stacking scanning. In the survey design, five isotropic sources or events (marked as red stars) in a row are embedded in the fifth layer and 240 receivers (marked as red triangles) in a star are distributed on the surface. We use the 3D acoustic finite difference to model the microseismic recordings (see Figure 5a). The stacking scanning algorithms with different conditions are applied in the true velocity model to search the location with the maximum energy in both temporal and spatial dimensions. The spatial energy distributions in space and time domains of three stack conditions are shown in Figure 3. The corresponding event locations presented in Figure 5b are all almost consistent with the true locations (marked by black dots), which indicates that three imaging conditions are all able to recover the event locations in this test.

Figure 3 shows that the energy maps of three imaging conditions in both time and space. Among the maps (Figure 3a, c and e) in temporal and (Figure 3b, d and f) in spatial dimensions, we can clearly observe that the energy map (Figure 3e) and (Figure 3f) are the most focused in the comparison to other maps. It means that the temporal and spatial resolutions obtained from the multi-cross-correlation condition are significantly higher than those obtained from both the linear and cross-correlation

conditions. Similarly, we also observe that the resolution of maps (Figure 3c and d) achieved by the cross-correlation condition is higher than those (Figure 3a and b) obtained from the linear condition. To further compare the resolutions of energy models, we extract the normalized energy images along three directions at the event location (1000 m, 1000 m, 1700 m), in Figure 4 we can obviously observe that the multi-cross-correlation condition (red lines) has the highest resolution, while the cross-correlation condition (blue lines) leads to a higher resolution than the linear condition (green lines) does. Compared to other two conditions, the multi-cross-correlation improves the imaging quality significantly.

Due to the nonexplosive feature or radiation pattern of most of the microseismic events, the polarity of the recorded waveform can be either positive or negative, which causes the maxima in the energy map do not correspond to the true source locations. Because the source mechanisms are usually represented by double couples (Kuang et al., 2016), we suppose to simulate the shear-slip source and set three geometry parameters (strike, dip, and rake) of the source as 90°, 45°, and 45°, respectively. The modeled waveforms with polarity reversals are displayed in Figure 6a. We employ the linear, cross-correlation, and multi-cross-correlation conditions to scan the waveform for the event location. In Figure 6b, the location errors (green squares) of the linear stacking illustrate that the location results deviate from the true location. However, the location results (blue crosses) of cross-correlation condition is almost not influenced. Additionally, we observe that the location results (red triangles) of the multi-cross-correlation condition are basically unaffected. Both cross-correlation and

multi-cross-correlation conditions effectively avoid the location uncertainty resulted from the polarity reversal.

The level of noise is a key indicator of the uncertainty in migration-based imaging of microseismic events. To test the uncertainty of event localization, we add three levels of Gaussian noises, 50%, 100%, and 150%, into the pure waveforms. The different levels of noisy data are displayed in Figure 7a, c, and e. The location error maps (Figure 7b, d, and f) present that both horizontal and vertical uncertainties increase with the component of Gaussian noise enhanced, especially for the vertical uncertainty. Through location errors, we can observe that the multi-cross-correlation is almost not influenced by the noisy data, since the multi-cross-correlation is capable of suppressing the noise when compared to other two conditions. Besides, the linear condition is the most sensitive to the noise among three stacking conditions.

FIELD DATA EXAMPLES

In this section, we apply our proposed conditions to the real waveform data for testing their efficiency. In Figure 8, we show two receiver geometries deployed on the surface to monitor the perforation shot and microseismic events, respectively. The perforation shot is recorded by 531 receivers, and the two survey lines are about 5000.0 m and 6000.0 m long, respectively (Figure 8b). We construct the initial P-wave velocity model from the well logging and calibrate the initial model utilizing the perforation shot to reduce the depth uncertainty. The calibrated velocity model is shown in Figure 8a. We use the calibrated model with the grid spacing of 10.0 m to scan the waveform data

from 0.1 s to 0.8 s with an interval of 2.0 ms. The true perforation position and its relocations using three conditions are shown in Table 1. The comparison with the true location shows that the calibrated P-wave velocity model is effective to recover the location of the perforation shot. For the horizontal location results, they all recover the true location of the perforation, while for the vertical location results, the multi-cross-correlation produces the most accurate result by comparing with other two results. We also display their corresponding temporal and spatial energy maps in Figure 9. We observe that the maps (Figure 9e and f) of the multi-cross-correlation condition have the highest resolution than other maps in both temporal and spatial dimensions. The synthetic move-out curve (red lines) of the best solution is also well matched with the first arrival waveform in Figure 10a, even though it is difficult to pick the arrival time manually.

The microseismic events induced by the hydraulic fracturing are recorded by 1788 receivers as shown in Figure 8b. The waveform data of one microseismic event is shown in Figure 10b. We select 20 effective microseismic events. The waveforms of the twenty events are similar and hence we infer that these events may be excited in the same region or along fractures with the similar mechanism. We calculate the traveltime table in the calibrated velocity model with the grid spacing of 10.0 m. Then we scan the waveform data respectively using three stacking conditions. In Figure 10b, we observe the scanned move-out curve (red lines) matches the first arrivals of the waveform well. We project all the location results into three plan maps (Figure 12a-c). From these maps, we recognize that the results (marked by green stars) of the linear condition are

scattered and a little far away from the production well, which may be attributable to the polarity reversals of recorded data. Nevertheless, the results of the cross-correlation and multi-cross-correlation seem more reasonable because they distribute more intensely and closely to the production well. Among three results, in terms of the distribution of the microseismic events, the results (red stars) of the cross-correlation and multi-cross-correlation conditions are the most reasonable and convincing. Because of high S/N of the selected events, we could not distinguish the obvious difference from the locations obtained from the cross-correlation and multi-correlation conditions.

DISCUSSIONS AND CONCLUSIONS

In this study, we introduce a cross-correlation condition for the stacking scanning algorithm by multiplying the amplitudes of neighboring receivers before summing up all the products during the stack, which is significantly different from the interferometric imaging (Li et al., 2015). To further enhance the resolution of location imaging and noise resistance, we further propose a multi-cross-correlation condition to stack recorded waveforms by directly multiplying amplitudes over single receiver or multiple adjacent receivers. From the equations in the section of methods, we can observe our proposed conditions are achieved by changing some computation operators on the basis of the conventional linear condition. Hence, the proposed conditions do not bring any extra computational cost on the scanning process compared to the linear condition.

In the comparison to the linear stack condition, both proposed stack conditions

enable the location image insensitive to the polarity reversals resulted from the non-explosive event. In the numerical experiments, we demonstrate the immunity of both proposed conditions to the polarity reversals in waveforms. We also analyze the location uncertainty from the low S/N of data. The multi-cross-correlation condition is superior to other two conditions on the noisy suppression (see Figure 7). Meanwhile, the multi-cross-correlation produces the most focused location image among three stack conditions. We further test the velocity uncertainty on the location results via these three conditions. The results are not presented in the numerical experiments. We find all three conditions are sensitive to the velocity perturbations. They almost result in the same vertical or depth location errors while horizontal locations are basically unaffected due to the dense receiver coverage on the surface for the local event location.

Because of the polarity reversals existed in the waveforms, the moment tensors need to be determined to correct the polarities in order for the true event location (i.e., Zhebel and Eisner, 2015; Liang et al., 2016). The common approach is to estimate event location and moment tensors simultaneously by means of the global optimization methods, such as the grid search method. These global optimization methods are such computational demanding that they can not applied in practice for real-time processing. With the proposed stack conditions, we are able to eliminate the effect of polarity reversals and skip the step of determinations of moment tensors in the common approach. Without searching for the moment tensors, the scanning stack algorithm with the proposed conditions may save much computational time, thereby having a potential for real-time location and even estimating moment tensors.

In the multi-cross-correlation stacking function, the receiver groups can be adjusted. As the number of receiver groups descends, the spatial resolution may decrease and the location uncertainty may arise. If all receivers are put in one group, then the location result is equivalent to that with the linear stack condition. The multi-cross-correlation condition is flexible that it is not quite subject to the receiver distribution, in other word, it is efficient in the sparse surface array, which is adaptive to monitor the natural micro-earthquake and beneficial for global seismology applications. Our field data example also shows that, compared with the linear condition, the cross-correlation and multi-cross-correlation conditions are robust and efficient to produce a more reasonable location result.

ACKNOWLEDGEMENTS

REFERENCES

Anikiev, D., Valenta, J., Staněk, F., Eisner, L. 2014. Joint location and source mechanism inversion of microseismic events: Benchmarking on seismicity induced by hydraulic fracturing. Geophysical Journal International, 198, 249-258.

Akram, J., Eaton, D. W. 2016. A review and appraisal of arrival-time picking methods for downhole microseismic data. Geophysics.

Artman, B., Podladtchikov, I., Witten, B. 2010. Source location using time-reverse imaging. Geophysical Prospecting, 58, 861-873.

Arfken, G. B., Weber, H. J., Harris, F. E. 2013. Mathematical methods for physicists, 7th ed.: Elsevier.

Baker, T., Granat, R., Clayton, R. W. 2005. Real-time earthquake location using Kirchhoff reconstruction. Bulletin of the Seismological Society of America, 95, 699-707.

Duncan, P. M., Eisner, L. 2010. Reservoir characterization using surface microseismic monitoring. Geophysics, 75(5), 75A139-75A146.

Eisner, L., Abbott, D., Barker, W. B., Lakings, J., Thornton, M. P. 2008. Noise suppression for detection and location of microseismic events using a matched filter. 80th Annual International Meeting, SEG, Expanded Abstracts, 1431-1435.

Eisner, L., Duncan, P. M., Heigl, W. M., Keller, W. R. 2009. Uncertainties in passive seismic monitoring. The Leading Edge, 28(6), 648-655.

Eisner, L., Hulsey, B. J., Duncan, P., Jurick, D., Werner, H., Keller, W. 2010. Comparison of surface and borehole locations of induced seismicity. Geophysical

Prospecting, 58(5), 809-820.

Feng, X., Chen, B., Li, S., Zhang, C., Xiao, Y., Feng, G., Chen, D. 2012. Studies on the evolution process of rockbursts in deep tunnels. Journal of Rock Mechanics and Geotechnical Engineering, 4(4), 289-295.

Fish, A. M. 2012. Microseismic velocity inversion and event location using reverse time imaging. Diss. Colorado School of Mines.

Gajewski, D., and Tessmer, E. 2005. Reverse modelling for seismic event characterization. Geophysical Journal International, 163(1), 276-284.

Gajewski, D., Anikiev, D., Kashtan, B., and Tessmer, E. 2007. Localization of seismic events by diffraction stacking: 77th Annual International Meeting, SEG, Expanded Abstracts, 1287-1291.

Geiger, L. 1912. Probability method for the determination of earthquake epicentres from the arrival time only. Bull. St. Louis Univ., 8, 60-71.

Got, J. L., Mourot, P., Grangeon, J. 2010. Pre-failure behaviour of an unstable limestone cliff from displacement and seismic data. Natural Hazards and Earth System Sciences, 10, 819-829.

Grechka, V., De La Pena, A., Schisselé-Rebel, E., Auger, E., Roux, P. 2015. Relative location of microseismicity. Geophysics, 80(6), WC1-WC9.

Grigoli, F., Cesca, S., Vassallo, M., Dahm, T. 2013. Automated seismic event location by travel-time stacking: An application to mining induced seismicity. Seismological Research Letters, 84, 666-677.

Haldorsen, J. B. U., Brooks, N. J., Milenkovic, M. 2013. Locating microseismic sources

using migration-based deconvolution. Geophysics, 78(5), KS73-KS84.

Han, S., Zhang, W., Zhang, J. 2015. Joint microseismic quasi-P and SH traveltime inversion for updating VTI parameters. 85th Annual International Meeting, SEG, Extended Abstract, 442-446.

Hulsey, B. J., Eisner, L., Thornton, M. P., Jurick, D. 2009. Application of relative location technique from surface arrays to microseismicity induced by shale fracturing. 79th Annual International Meeting, SEG, Expanded Abstracts, 1602-1606.

Jarillo Michel, O., Tsvankin, I. 2014a. Gradient calculation for waveform inversion of microseismic data in VTI media. Journal of Seismic Exploration, 23(3), 201-217.

Jarillo Michel, O., Tsvankin, I. 2014b. Waveform inversion for parameters of microseismic sources in VTI media. 84th Annual International Meeting, SEG, Expanded Abstracts, 1045-1048.

Kao, H., Shan, S. J. 2004. The Source-Scanning Algorithm: mapping the distribution of seismic sources in time and space. Geophysical Journal International, 157, 589-594.

Kao, H., Shan, S., Dragert, H., Rogers, G., Cassidy, J. F., Wang, K., James, T. S., James, Ramachandran, K. 2006. Spatial-temporal patterns of seismic tremors in northern Cascadia. Journal of Geophysical Research, 111, B03309.

Kuang, W., Zoback, M., Zhang, J. 2016. Estimating geomechanical parameters from microseismic plane focal mechanisms recorded during multistage hydraulic fracturing. Geophysics, 82(1), KS1-KS11.

Li, Z., Zhao, B. 2012. Microseism monitoring system for coal and gas outburst: International Journal of Computer Science Issues, 9, 24-28.

Li, J., Li, C., Morton, S. A., Dohmen, T., Katahara, K., Toksöz, M. N. 2014. Microseismic joint location and anisotropic velocity inversion for hydraulic fracturing in a tight Bakken reservoir. Geophysics, 79(5), C111-C122.

Li, L., Chen, H., Wang, X. 2015. Weighted-elastic-wave interferometric imaging of microseismic source location. Applied Geophysics, 12(2), 221-234.

Liang, C., Yu, Y., Yang, Y., Kang, L., Yin, C., Wu, F. 2016. Joint inversion of source location and focal mechanism of microseismicity. Geophysics, 81(2), KS41-KS49.

Liao, Y. C., Kao, H., Rosenberger, A., Hsu, S. K., Huang, B. S. 2012. Delineating complex spatiotemporal distribution of earthquake aftershocks: An improved source-scanning algorithm. Geophysical Journal International, 189, 1753-1770.

McMechan, G. A. 1982. Determination of source parameters by wavefield extrapolation. Geophysical Journal International, 71(4), 613-628.

Michel, O. J., Tsvankin, I. 2016. Anisotropic waveform inversion for microseismic velocity analysis and event location. 86th Annual International Meeting, SEG, Expanded Abstracts, 296-300.

Minkoff, S. E., Symes, W. W. 1997. Full waveform inversion of marine reflection data in the plane-wave domain. Geophysics, 62(2), 540-553.

Mueller, M. 2013. Meeting the challenge of uncertainty in surface microseismic monitoring. First Break, 31(7), 89-95.

Ramos-Martínez, J., McMechan, G. A. 2001. Source-parameter estimation by full

waveform inversion in 3D heterogeneous, viscoelastic, anisotropic media. Bulletin of the Seismological Society of America, 91(2), 276-291.

Ramachandran, K. 2006. Spatial-temporal patterns of seismic tremors in northern Cascadia. Journal of Geophysical Research.

Rentsch, S., Buske, S., Lueth, S., Shapiro, S. 2007. Fast location of seismicity: A migration-type approach with application to hydraulic-fracturing data. Geophysics, 72(1), S33-S40.

Roman, D. C., Cashman, K. V. 2006. The origin of volcano-tectonic earthquake swarms. Geology, 34, 457-460.

Rutledge J., Phillips W. 2003. Hydraulic stimulation of natural fractures as revealed by induced microearthquakes, Carthage Cotton Valley gas field, East Texas. Geophysics, 68(2), 441-452.

Suckale, J. 2009. Induced seismicity in hydrocarbon fields. Advances in geophysics, 51, 55-106.

Schuster, G., 2009, Seismic interferometry: Cambridge University Press.

Tian, X., Zhang, W., Zhang, J. 2016. Joint inversion of perforations and Microseismic events. 78th EAGE Conference and Exhibition.

Thornton, M., Eisner, L. 2011. Uncertainty in surface microseismic monitoring. 81st Annual International Meeting, SEG, Expanded Abstracts, 1524-1528.

Vlček, J., Fischer, T., Vilhelm, J. 2016. Back-projection stacking of P- and S- waves to determine location and focal mechanism of microseismic events recorded by a surface array. Geophysical Prospecting, 64(6), 1428-1440.

Witten, B., Artman, B. 2012. Signal-to-noise estimates of time reverse images. Geophysics, 76(2), MA1-MA10.

Wu, Y., McMechan, G. A. 1996. Elastic full-waveform inversion for earthquake source parameters. Geophysical Journal International, 127(1), 61-74.

Wu, S., Wang, Y., Zheng, Y., Chang, X., 2017. Microseismic source locations with deconvolution migration. Geophysical Journal International, 212(3), 2088-2115.

Zhang, W., Zhang, J. 2013. Microseismic migration by semblance-weighted stacking and interferometry. 83rd Annual International Meeting, SEG, Expanded Abstracts, 2045-2049.

Zhebel, O., Eisner, L. 2014. Simultaneous microseismic event localization and source mechanism determination. Geophysics, 80(1), KS1-KS9.
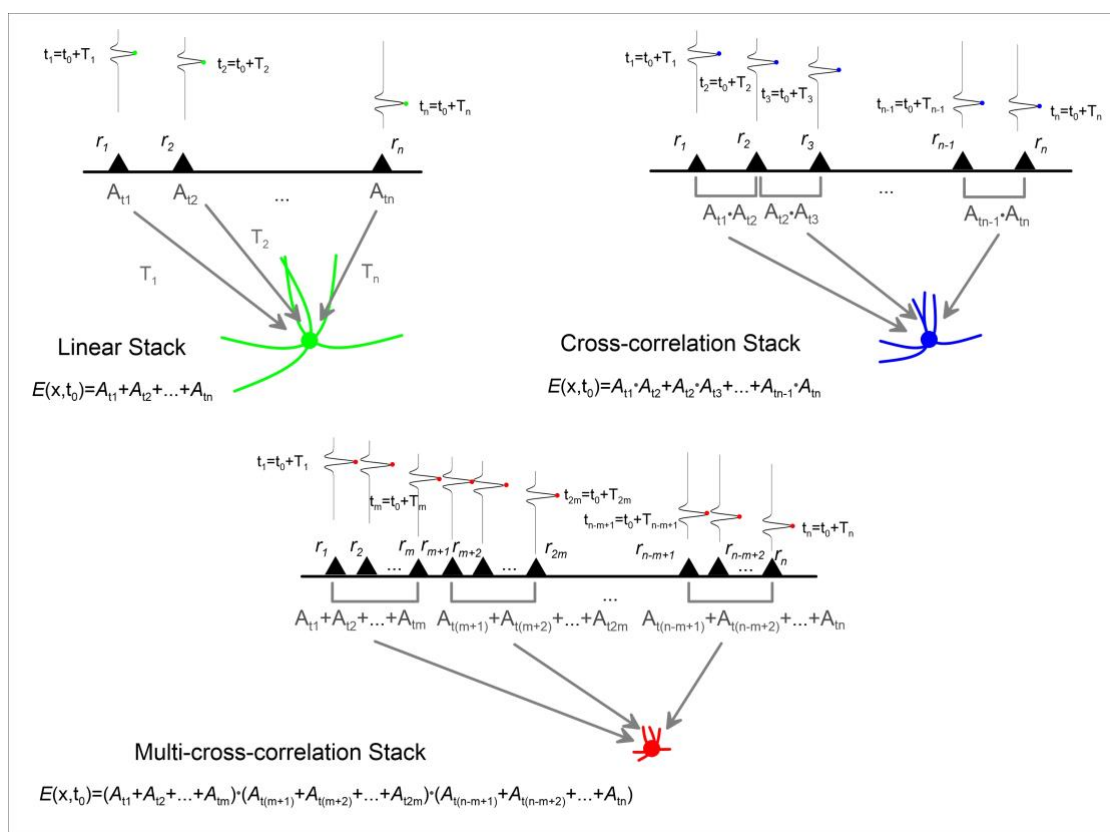
Figure 1: A schematic diagram to illustrate the concepts of three stacking conditions. The energy E of a point X at a time t_0 can be calculated by these conditions from all stations at the predicted arrival times t (t_0 plus the respective traveltimes T_1, T_2, and T_n, as marked by dots). n represent the total number of receivers. m denotes the number of receivers in each group in the multi-cross-correlation stack condition. A bright spot (marked by filled circles) is found if its location and time are consistent with the arrival time of the largest amplitude A_t at each station. Green, blue, and red represent the linear, cross-correlation, and multi-cross-correlation stacking conditions, respectively. Those arcs across the filled circles denote the artifacts along with the true location points. The artifacts are more obvious with the longer arcs, which illustrates that both two latter conditions reduce the imaging artifacts and improve the resolution of the location image.

a)

b)
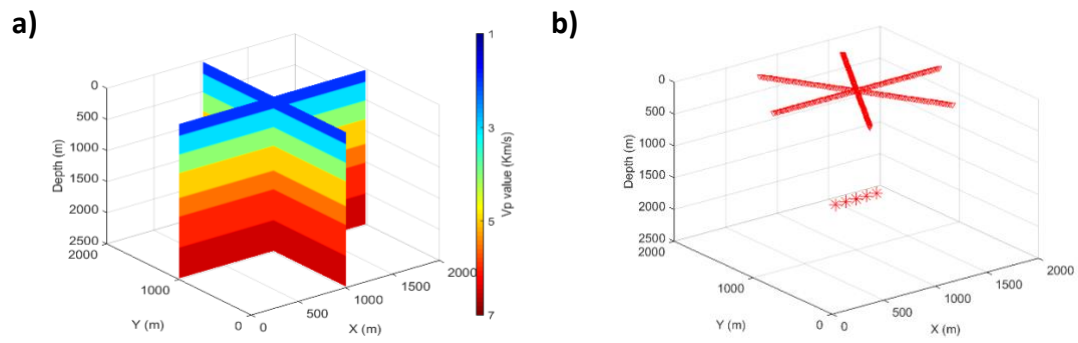
Figure 2: (a) The 1D velocity model with seven layers. (b) The survey geometry with 240 receivers (red triangles) distributed on the surface and five events marked by red stars.
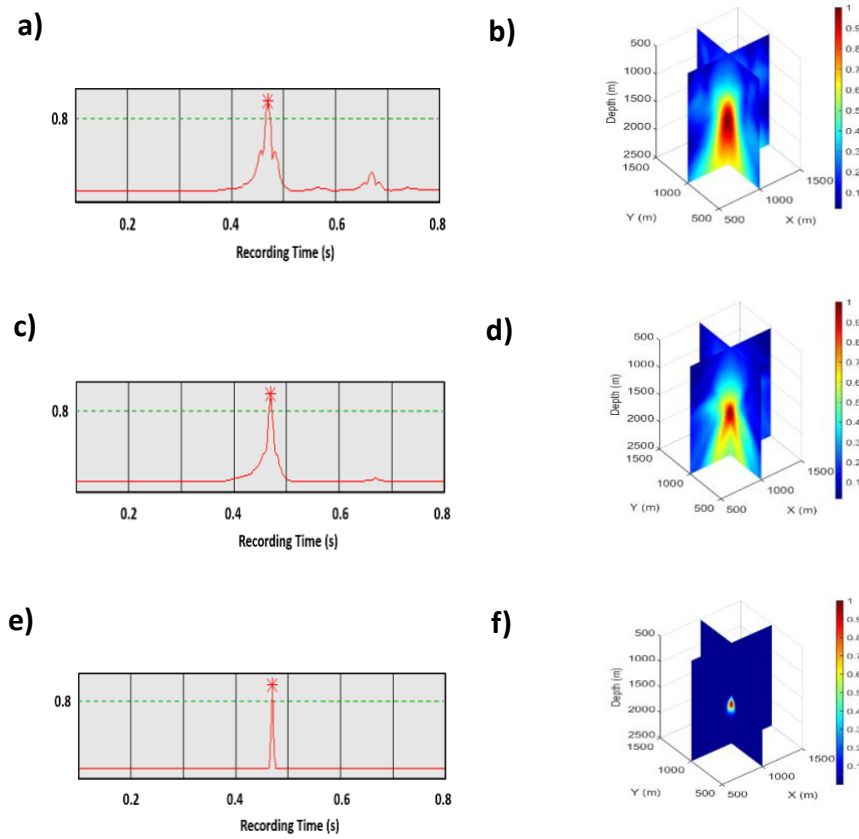
Figure 3: The temporal maximum energy maps (a, c, e) and spatial energy maps (b, d, f) of the event (1000 m, 1000 m, 1700 m). (a, b), (c, d), and (e, f) are the energy maps obtained by using the linear, cross-correlation, and multi-cross-correlation conditions, respectively.
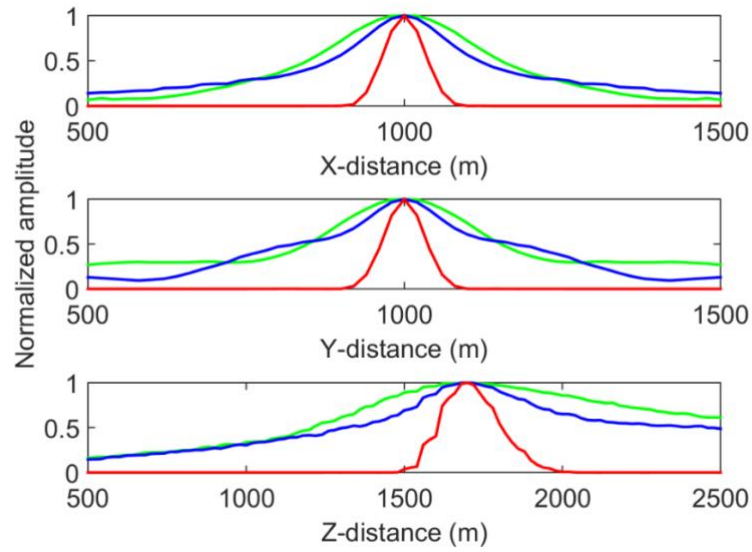
Figure 4: The normalized image results extracted from the images in Figure 2 along different directions at the event location (1000 m, 1000 m, 1700 m). Green, blue, and red lines represent the image results with the linear, cross-correlation, and multi-cross-correlation conditions, respectively.
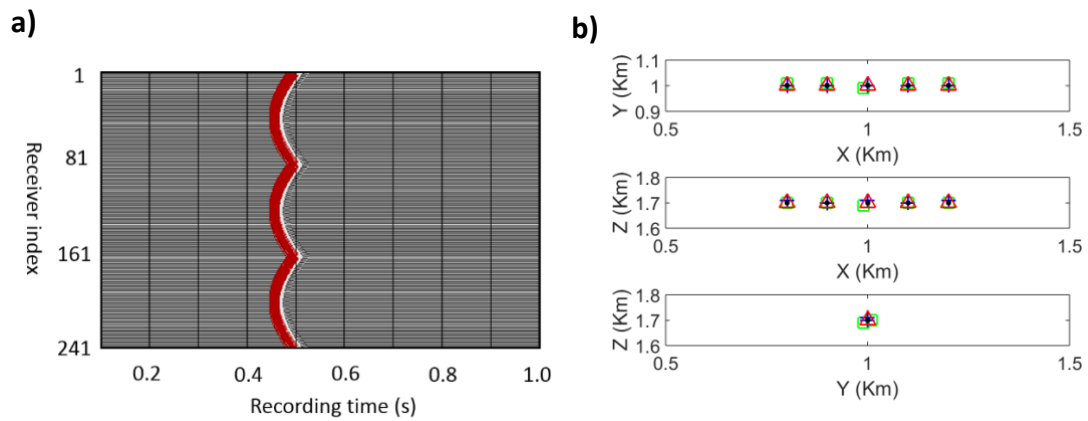
Figure 5: (a) The waveform data produced by the third event located at (1000 m, 1000 m, 1700 m) and the red curve represents the arrival time curve of the best solution. (b) The five location results scanned by the linear (green square), cross-correlation (blue cross), and multi-cross-correlation (red triangle) conditions. The black dots are the true locations.
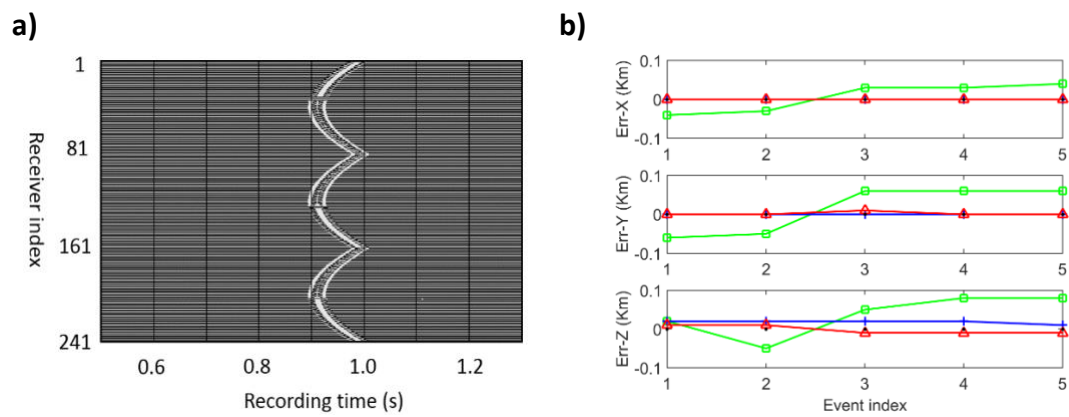
Figure 6: (a) The waveform data with polarity reversal simulated using a shear source, its fault geometries (strike, dip, and rake) equal to 90°, 45° and 45°. (b) The absolute errors of location results with three stack conditions. The green squares, blue crosses, and red triangles are the events located by the linear, cross-correlation, and multi-cross-correlation conditions. The black dots denote the true locations.
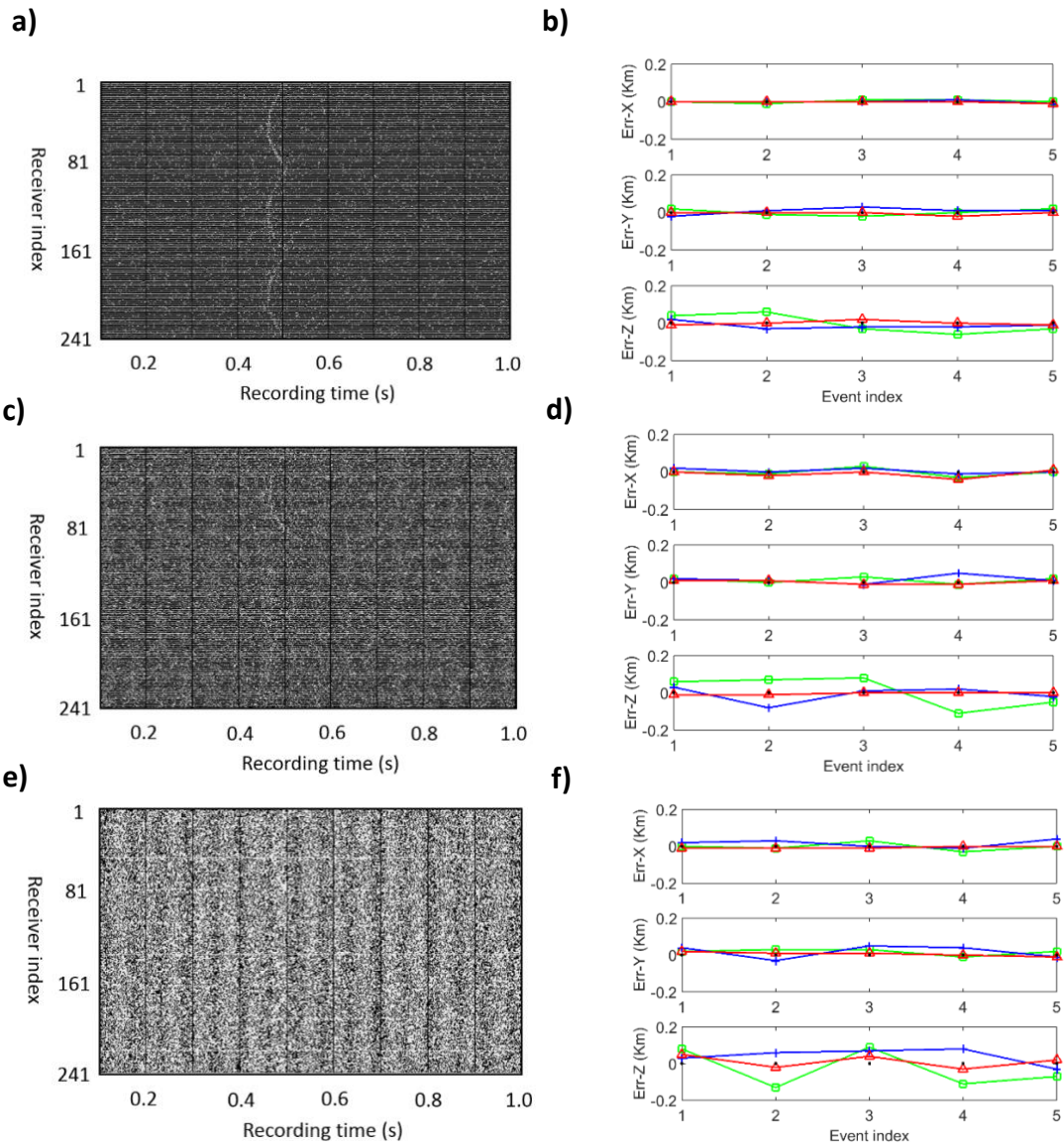
Figure 7: The contaminated waveform data added with 50% Gaussian noise (a), 100% Gaussian noise (c) and 150% Gaussian noise (e). The corresponding absolute errors (b, d, f) of all event locations to (a, c, e), respectively. The green squares, blue crosses, and red triangles are the events located by the linear, cross-correlation, and multi-cross-correlation conditions. The black dots are the true locations.
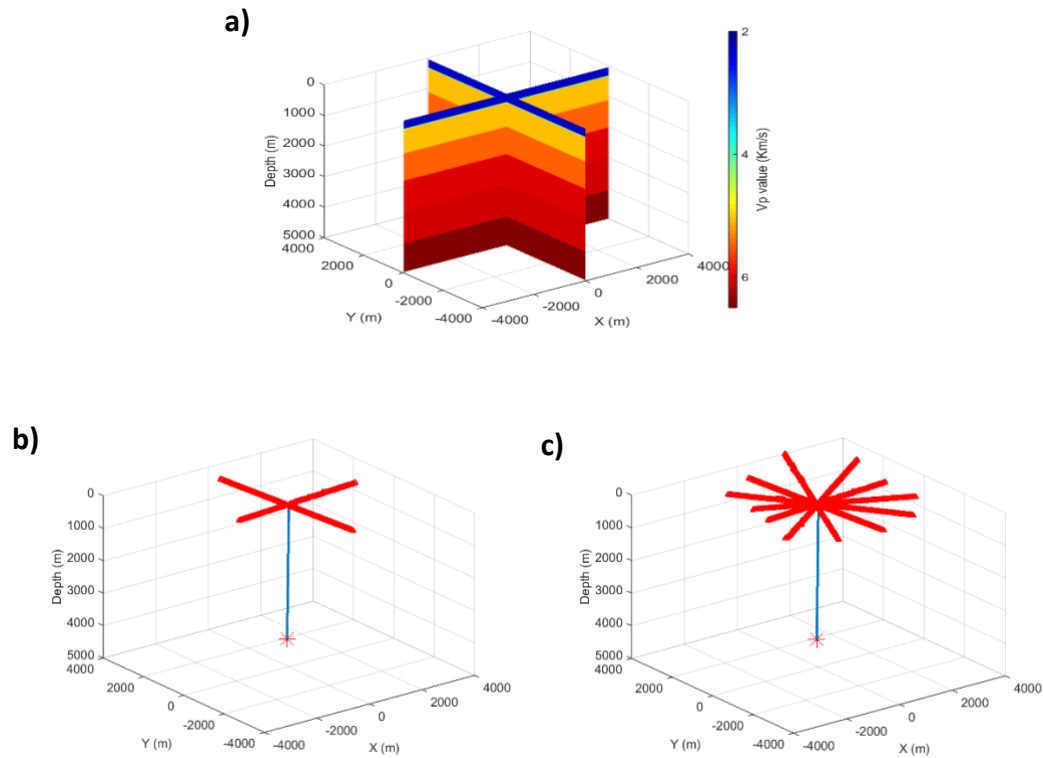
Figure 8: (a) The velocity model used for the stacking scanning. (b) The receiver geometry for the perforation shot. (c) The receiver geometry designed for the microseismic events induced by hydraulic fracturing. The red triangles are the distributed receivers. The blue line is the production well. And the red star represents the perforation shot.
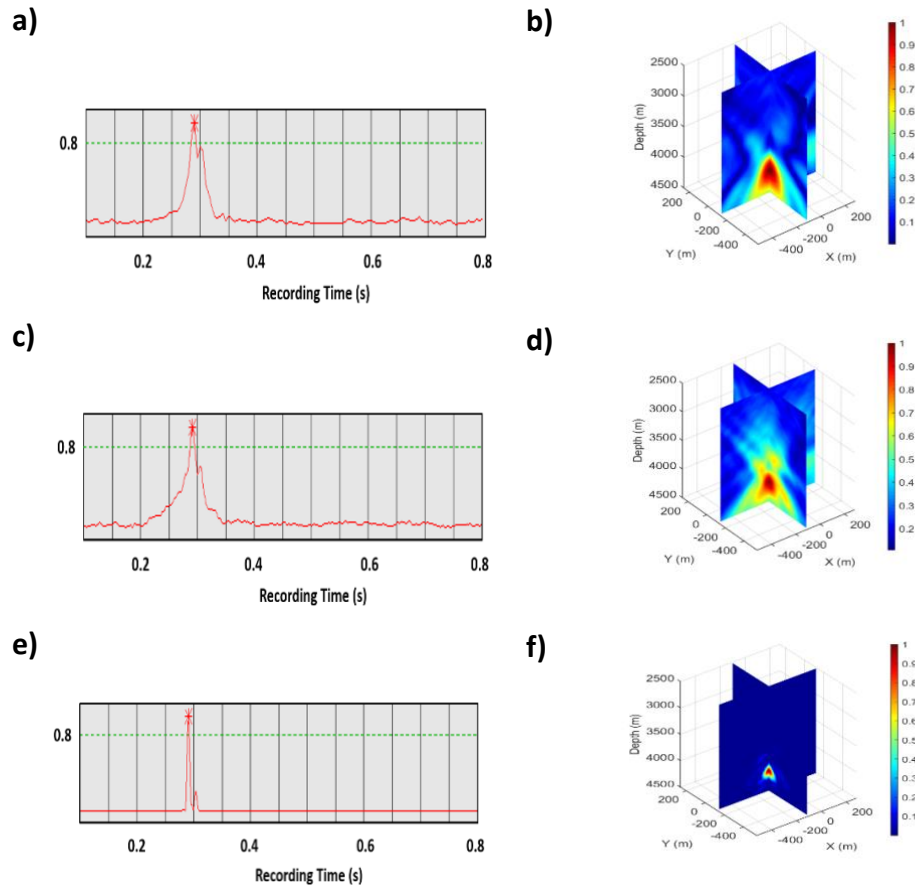
Figure 9: The temporal maximum energy maps (a, c, e) and spatial energy maps (b, d, f) of the perforation shot. (a, b), (c, d), and (e, f) are the energy maps obtained by using the linear, cross-correlation, and multi-cross-correlation conditions, respectively.
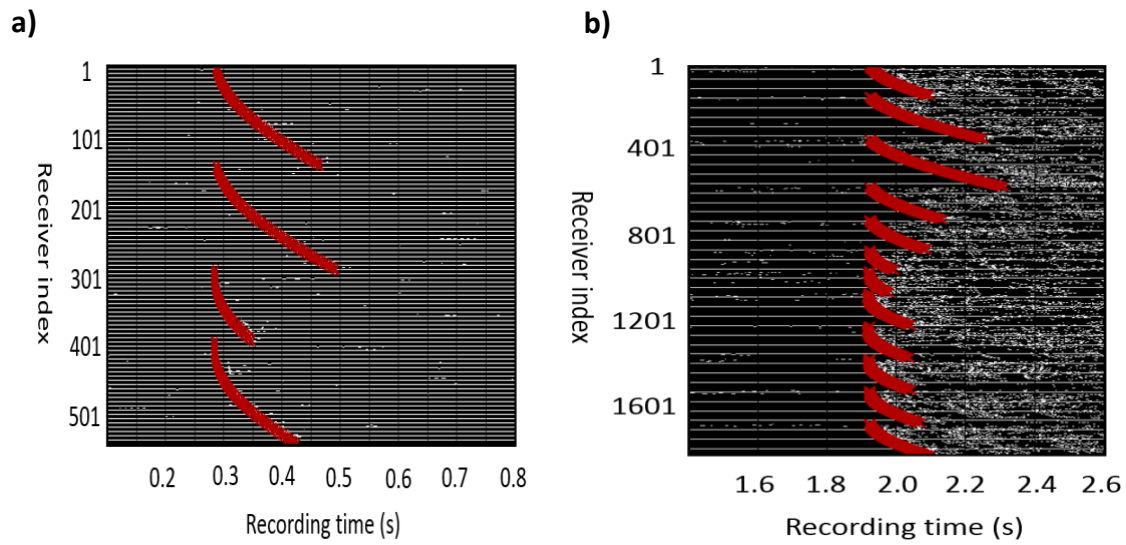
Figure 10: (a) The waveform data of the perforation shot and the move-out curve (red lines) of the best solution (-110 m, 140 m, 4110 m). (b) The waveform data of the microseismic event and the move-out curve (red lines) of the best solution (-460 m, -340 m, 4440 m).
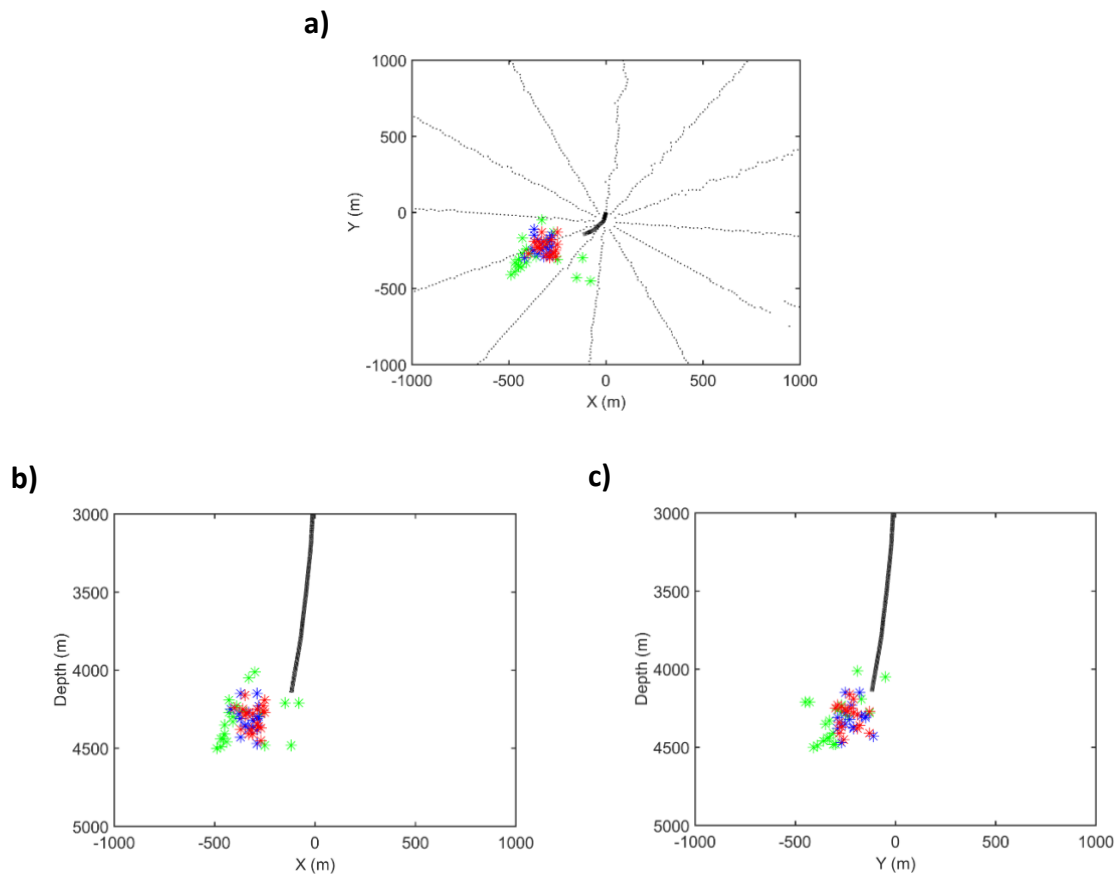
Figure 11: The location results of 20 events using three stacking conditions. The green, blue and red stars are the events located respectively by the linear, cross-correlation, and multi-cross-correlation conditions. The black dots and line are the receivers and production well, respectively. (a-c) represents different plan views of event locations.

Table 1: The true location of the perforation shot and the corresponding relocation results using the linear, cross-correlation, and multi-cross-correlation conditions.

	X (m)	Y (m)	Depth (m)
True	-110.94	-141.33	4087.8
Linear	-110.0	-140.0	4110.0
Cross-correlation	-110.0	-140.0	4060.0
Multi-cross-correlation	-110.0	-140.0	4080.0